Crystallization of Mesoporous Metal Oxides†

Junko N. Kondo*,‡ and Kazunari Domen§

Chemical Resources Laboratory, Tokyo Institute of Technology R1-10, 4259 Nagatsuta, Midori-ku, Yokohama 226-8503, Japan, and Department of Chemical System Engineering, The University of Tokyo, 7-3-1 Hongo, Bunkuo-ku, Tokyo 113-8656, Japan

Received August 3, 2007. Revised Manuscript Received November 10, 2007

Crystallization of an amorphous inorganic network of mesoporous metal oxides is achieved while maintaining the original ordered mesoporous structure. The methodology utilizes reinforcement (carbon or silica) to strengthen the periodic structure so that the original ordered mesoporous structure is preserved during thermal treatment for crystallization. The reinforcement is removed after crystallization to provide crystalline mesoporous metal oxide with the original ordered structure. Enhancement of photocatalytic activity for the total decomposition of water over mesoporous Ta_2O_5 after crystallization is shown as an example of the advantages of crystalline mesoporous metal oxides.

1. Introduction

Solids can be classified into two categories, crystalline and amorphous.[1] A crystalline solid possesses rigid and long-range order, where its atoms, molecules, or ions occupy specific positions. The most stable form for solids is the crystalline form. However, if a solid is formed by quenching of its liquid phase, its atoms or molecules do not have sufficient time to arrange in the most stable positions, and they become frozen in positions other than those of a regular crystal. The resulting solid is said to be amorphous. Amorphous solids, represented by glass, lack a well-defined three-dimensional arrangement and long-range ordering of atoms. Considering only inorganic substances, amorphous solids are also formed by well-known sol–gel methods, which are applied in the low-temperature range. In such cases, atoms or molecules are not supplied sufficient thermal energy to overcome the activation energy required to change their positions within the solid. In other words, thermal treatment in a sufficiently high temperature range converts the internal structure of the solid from amorphous to crystalline, which accompanies a drastic mass transfer and usually results in increasing density. A crystalline inorganic solid is conventionally defined as possessing a unit cell, which is the basic repeating structural unit of the crystalline solid, at a subnanometer (angstrom) scale, except for zeolites. On the other hand, the emergence of liquid crystal templating methods for the preparation of mesoporous materials has extended the above-defined size of the unit cell to the nanometer scale. Nanometer-sized mesopores are periodically arranged with various symmetries in many inorganic solids. Although the inorganic materials themselves are amorphous, such mesoporous materials are sometimes regarded as crystalline because of the presence of X-ray diffraction (XRD) peaks in the small-angle region.[2] To avoid confusion, we limit the term "crystalline" in this article to the arrangement of positions of atoms or ions in solids at a subnanometer scale. Thus, the examined solids in this article are required to consist of a crystalline inorganic phase with coexistent nanometer-sized pores. Consequently, assemblies of nanocrystalline primary particles, where pores are attributed to interparticle voids, are distinguished. Because of their general applications, recent review articles are cited as references for crystalline mesoporous Al_2O_3[3] and TiO_2,[4] which possess uniformly nanosized interparticle spaces.

Crystalline mesoporous oxides reported so far are grouped into periodic organosilicas,[5] zeolites, and metal oxides.[6,7] Here, the latter, crystallized mesoporous metal oxides, are fully explained using experimental data we obtained. The amorphous pore walls of most mesoporous materials, which offer only poor thermal and mechanical stability, restrict the range of application of these materials. However, a crystallized wall structure can be expected to provide better thermal and mechanical stability, as well as superior electric and optical properties. In addition, the presence of a crystallized wall structure would cause the appearance of specific electronic orbitals and lattice defects that are frequently responsible for catalysis and that are notably absent in amorphous materials. The crystallization and crystallinity of mesoporous materials have therefore attracted much attention. Therefore, methods are introduced for the preparation of crystalline mesoporous metal oxides, so as to involve mesopores within single-crystal domains.

2. Preparation of Amorphous Mesoporous Metal Oxides

A general method for the preparation of mesoporous metal oxides was reported in the late 20th century.[8,9] Whereas other methods use electrostatic interaction between ionic structure-directing agents (SDA) and inorganic precursors,[10] the general preparation method utilizes hydrophilic−hydrophobic interaction between SDA and metal precursors; the hydrophilic moiety of neutral block copolymers affects the

* Corresponding author. E-mail: jnomura@res.titech.ac.jp.
† Part of the "Templated Materials Special Issue".
‡ Tokyo Institute of Technology.
§ The University of Tokyo.

10.1021/cm702176m CCC: $40.75
Published on Web 12/29/2007

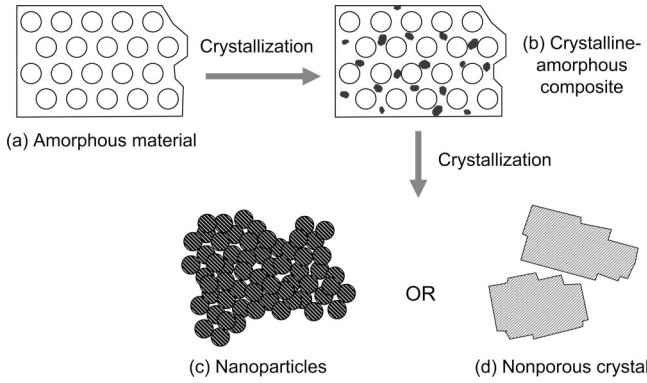

Figure 1. Scheme for the crystallization of mesoporous metal oxides.

inorganic precursors in a hydrophilic solvent, so that the hydrophobic parts are enclosed inside micelles. The employment of hydrophilic−hydrophilic interaction and hydrophilic−hydrophobic separation for the creation of a mesostructure enables various metal oxides to include mesopores with two-dimensional hexagonal (2D-hex) structure in the inorganic solid phase. After calcination for the removal of the template, amorphous mesoporous metal oxides are obtained. However, in the case of a metal oxide with a low crystallization temperature, small crystalline patches are formed in the amorphous phase during thermal treatment. Through the crystalline−amorphous composite (Figure 1b), the mesoporous structure is lost because of crystallization occurring at the temperature required for complete removal of the template (parts c and d in Figure 1). Strategies for obtaining such crystallized materials by direct calcination are summarized in Section 6, whereas crystallization methods for amorphous mesoporous metal oxides are described first in Section 4, and one example of an application of crystallized mesoporous metal oxide is given in Section 5.

Modified preparation methods for mesoporous transition metal oxides, amorphous precursors for crystallization, are described elsewhere.[11−14] Briefly, triblock copolymers P123 ($HO(CH_2CH_2O)_{20}(CH_2CH(OH)CH_2O)_{70}(CH_2CH_2O)_{20}H$) for Ta, Nb, and their mixed oxides or P85 ($HO(CH_2CH_2O)_{39}$-$(CH_2CH(OH)CH_2O)_{26}(CH_2CH_2O)_{39}H$) for Ti mixed oxides are used as the SDA, and 1 g of SDA is dissolved in 10 g of ethanol or propanol solvent, respectively, at room temperature. To this solution is added 6–10 mmol of metal precursors with vigorous stirring. Water (6–70 mmol) or aqueous hydrochloride (37%, 10 mmol) is added to the solution with further stirring. The resulting sol is gelled in a Petri dish at 40 °C for 3–14 days. The aged gel samples are then calcined at 350–500 °C for 5–10 h in air for removal of the SDA.

3. Crystallization by Calcination in Air

When the amorphous mesoporous metal oxides are crystallized by calcination in air, the result is assemblies of nanoparticles or nonporous crystals through the crystalline amorphous composite (Figure 1). The presence of SDAs has no more effect after crystallization in the latter case, and the same nonporous crystals are produced by a conventional sol–gel method without SDA. The former nanoparticle assemblies show larger mesopores from N_2 adsorption–desorption isotherms than from their amorphous precursors because of the spaces among the nanosized crystals. It is worth noting that for the crystallization of mesoporous Al_2O_3, calcination at 1000 °C results in different crystalline phases and pore sizes with similar BET surface areas, depending on the preparation method of the amorphous mesoporous precursors.[3] In contrast to mesoporous SiO_2, high-temperature treatment of Al_2O_3 induces crystallization. Thus, considering requirements for application as a catalyst–support, it is important to understand the changes in the size and structure of mesopores in mesoporous Al_2O_3, as well as the crystallization behavior during thermal treatment.[3]

In nanoparticle assemblies (Figure 1c), the expanded apparent pores are present outside the crystals, whereas for the amorphous precursors, the pores are present inside the inorganic solid. For general solid catalysis, where the chemical and physical states of the surface are essential, it is not so important whether the pores are inside or outside the crystals. However, when it comes to electron conductivity, magnetic properties, sensing capacity, photocatalytic performance, and so on, the continuity of the inorganic phase, size of single crystals, and the three-dimensional relation between the space and the crystals are crucial. The details of the relation between crystal phases and pores are clarified by transmission electron microscopy (TEM) and electron diffraction (ED). The structure and direction of a single crystal domain are found by direct observation of lattice fringes in high-resolution images, where the positions of the spaces relative to the lattice fringes are also observed. ED patterns from selected areas enable approximate estimation of the size of single-crystal domains, and the crystal-space relation is described by the sizes of pores and crystals. The destiny of amorphous mesoporous materials to be crystallized into either nanoparticle assemblies or nonporous crystals (Figure 1) is determined by the balance of the rate of nucleation and the rate of crystal growth, which is not thoroughly understood.

As a rare case, mesoporous single crystals were obtained for Nb and Ta mixed oxide, whereas pure mesoporous Nb and Ta oxides resulted only in the destruction of the porous structures upon crystallization at 400 and 750 °C, respectively.[15,16] The mixing ratio of Nb and Ta (Nb:Ta) mixed oxides to form mesoporous single crystals after calcination ranges from 1:9 to 9:1, and the crystallization temperatures estimated from thermogravimetry/differential thermal analysis (TG-DTA) linearly change between those of pure Nb and Ta oxides. Thus, Nb and Ta atoms are homogeneously mixed in the oxide phase. The first mesoporous single crystals were obtained from amorphous Nb−Ta mixed oxide with random mesoporous structure. Because the changes of the oxide, with regard to atomic position as well as mesostructure, are not observed when the change is from one random phase to another, ordered mesoporous Nb−Ta was prepared and examined. Mesoporous Nb−Ta mixed oxide with 2D-hex structure,[17] shown in Figure 2a, was crystallized next by calcination in air at 650 °C. Despite the structure of the amorphous precursor, single-crystal particles were formed

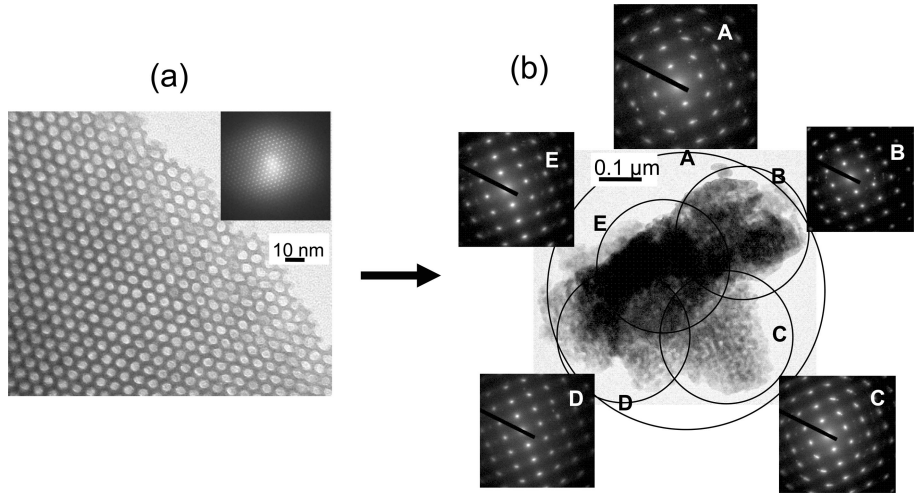

Figure 2. TEM images and ED patterns of mesoporous $(Nb,Ta)_2O_5$, before and after crystallization by calcination in air. (a) Amorphous $(Nb,Ta)_2O_5$ and (b) single-crystal $(Nb,Ta)_2O_5$. Zones indicated by A−E are selected areas.

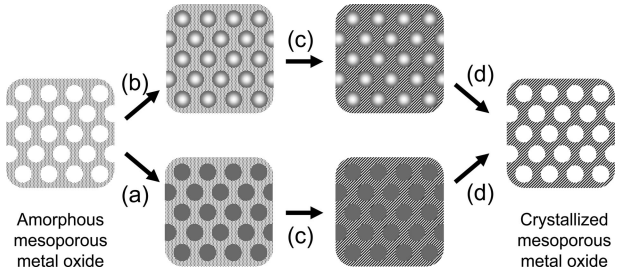

Figure 3. Schematic illustration of the strategy for reinforced crystallization of mesoporous metal oxides: (a) back filling, (b) coating, (c) crystallization, and (d) removal of the reinforcement.

in which mesopores were running through the particle without any ordered structure.[18] As shown in the TEM image of Figure 2b, mesopores are randomly arranged in a particle of submicrometer size. The spot ED pattern observed for the entire particle (A) indicates the presence of a sole crystal domain. Four ED patterns, collected from each part (B−E) of the particle are identical to pattern (A), indicating that the entire mesoporous particle observed is a single crystal. Although porous spaces are assured in crystal domains, the original ordered mesoporous structure has disappeared. In addition, this type of crystalline mesoporous material is valid only for Nb−Ta mixed oxides. Thus, to preserve the original mesoporous structure after crystallization, we should devise any strategy to reinforce the pore walls, as described below.

4. Reinforcement of Pore Walls

Figure 3 illustrates the general concept for reinforcement of the pore walls, in order to survive the structural transition during crystallization. In one method, the inside of the mesopores of the amorphous precursor are filled with carbon, e.g., in procedure (a), followed by calcination in inert atmosphere for crystallization. The filler carbon is then removed by calcination in air, similarly to the template removal for the amorphous metal oxides. The other method is to strengthen the structure by coating; the internal and external surfaces of amorphous materials are covered by silica layers with a certain thickness (procedure (b)). After crystallization by calcination in air, the silica layers are removed by treatment with alkaline solution.

4.1. Carbon Filling Consolidation. A nanoporous carbon material with hexagonal mesoporous structure is formed by filling carbon into a mesoporous silica material followed by silica etching.[19] The mesoporous silica used is SBA-15, which is prepared with a triblock copolymer P123. Because the same SDA is used for SBA-15 and metal oxide mesoporous materials, carbon is expected to be similarly filled into the mesopores of metal oxides. A Nb−Ta mixed oxide with 2D-hex mesoporous structure is first applied to evaluate the effect of the presence of carbon during crystallization, in comparison with the formation of the above-mentioned single crystal random mesoporous material. 2-Furanmethanol (furfuryl alcohol) vapor in N_2 gas is passed through the amorphous precursor in a fixed reactor at 200 °C for 2 h. The polymerized 2-furanmethanol is carbonized at 550 °C for 3 h under a vacuum. The sample is subsequently crystallized by heating in a He atmosphere at 650 °C, followed by removal of the carbon template from the crystallized sample by calcination at 500 °C in air.[20]

Figure 4 shows comparisons of the small- and wide-angle XRD patterns for mesoporous Nb−Ta mixed oxide samples with the aid of carbon reinforcement before and after crystallization, together with N_2 adsorption–desorption isotherms. In the small-angle XRD pattern, a peak attributed to the 2D-hex mesoporous structure shifts from 7.4 to 6.8 nm after crystallization, which is confirmed by the emergence of some peaks assigned to crystallized Nb−Ta mixed oxide. Pure Nb and Ta oxides have a similar orthorhombic crystal structure and their wide-angle XRD patterns are similar to that observed in Figure 4B. Three main peaks between 20 and 40° in Figure 4B appear at angles corresponding to those between pure Nb and Ta oxides. Therefore, in the crystallized mesoporous Nb−Ta oxide, the two metal components are regarded as being homogeneously mixed. Although the original ordered 2D-hex mesoporous structure is observed in a single-crystal domain in some places of the TEM sample, comparison of the N_2 adsorption–desorption isotherms of

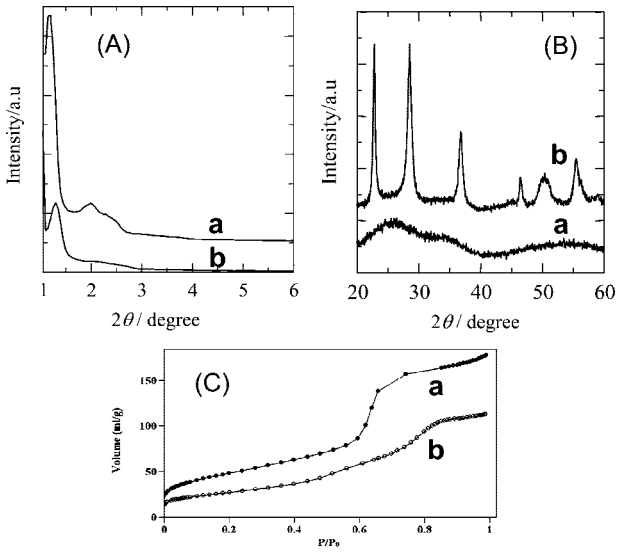

Figure 4. (A) Small- and (B) wide-angle XRD patterns and (C) N_2 adsorption isotherms of mesoporous $(Nb,Ta)_2O_5$ (a) before and (b) after crystallization.

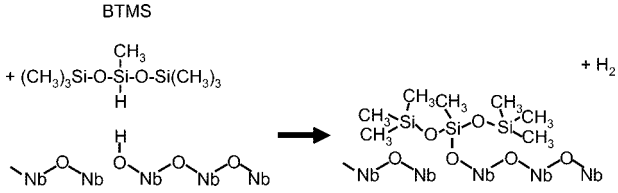

Figure 5. Reaction of hydroxyl groups with BTMS.

samples before and after crystallization (Figure 4C) provides an estimate of the yield of this somewhat crystallized part to be from one-quarter to one-third. The BET surface area and pore volume decrease from 184 to 94 $m^2\ g^{-1}$ and from 0.34 to 0.23 mL g^{-1}, respectively, after crystallization.

Because the original ordered mesoporous structure is not perfectly retained after crystallization with a carbon filling, the formation of a carbon replica is not considered to be completed in the mesopores of the Nb−Ta oxide. It should be mentioned that the carbon-filling method depends greatly on the surface character of the material; it is not applicable to oxides that are nonresistant to acids or to hydrophobic materials. Although the employment of some structure-strengthening substances is found to be beneficial, more general and milder conditions are required.

4.2. Silica-Coating by BTMS Accumulation. Surface hydroxyl groups of oxides react with various chemical reagents, and the reactions are used for modification of solid surfaces. Silylation of a mesoporous metal oxide surface is reported for Sn oxide, where hexamethyldisilazane (HMDS, $(Si(CH_3)_3)_2NH$) is reacted with surface hydroxyl groups.[21] Among the various silicone compounds attempted, bis-trimethylsiloxy-methylsilane (BTMS; $(CH_3)_3Si\text{-}O\text{-}SiH(CH_3)\text{-}O\text{-}Si(CH_3)_3$) is the most advantageous for fortification of the pore walls against mass transfer upon crystallization. A family of Si−H bond-possessing silicone compounds is used to estimate the amount of surface hydroxyl groups on metal oxides by quantification of the evolved hydrogen (Figure 5). The reacted, attached, or adsorbed (see below) BTMS on the surfaces of mesoporous metal oxides is converted to silica by calcination. The combustion of the organic groups of BTMS introduced inside and outside the pores is indicated by an exothermal peak with a remarkable weight loss at around 550 °C in the TG-DTA curves. In this way, a silica layer is formed during temperature increase for crystallization and at a lower temperature than that required for crystallization of the inorganic phase.

The detailed modification conditions were determined for mesoporous Nb oxide; therefore, the optimization is described using mesoporous Nb oxide as an example. First, for the efficient reaction of BTMS with the surface hydroxyl groups of mesoporous Nb oxide, elimination of adsorbed water was rigorously performed in order to activate the hydroxyl groups for the reaction in toluene as a solvent. The toluene and excess BTMS was removed after the reaction using tetrahydrofuran (THF). By this treatment, only BTMS molecules anchored at the position of surface hydroxyl groups on the mesoporous Nb oxides remain by the formation of Nb−O−Si bonds. The sample was then calcined in air to induce crystallization, during which a thin silica layer is formed (Figure 6a). By forming thin silica layers, the crystallization temperature increased, which was estimated by an exothermal DTA peak from 603 to 642 °C without any weight loss. Thus, the crystallization of the BTMS-modified sample was performed at 642 °C. To remove the silica layer, the crystallized mesoporous Nb oxide is finally treated three times with alkaline solution (pH 13) at 100 °C for 10–20 min each time. Large mesopores are indicated by the N_2 adsorption–desorption isotherms of the obtained crystallized Nb oxide. The larger pores were not present in crystal domains, but were found to be interparticle spaces between typical assemblies of nanoparticles, as shown by the TEM images and ring ED patterns of approximately 100 nm diameter range.

Next, to further strengthen the structure by forming thick layers of silica onto mesoporous Nb oxide, we performed only a brief dehydration by evacuation of the amorphous sample at 70 °C, followed by addition of pure liquid BTMS. The BTMS monomers, which are not involved in any reactions or adsorption, are removed by evacuation. In addition to the BTMS reacting with the surface hydroxyl groups, weakly adsorbed BTMS, as well as byproducts of the self-reactions of BTMS, remained on the Nb oxide surface. As a result of inclusion of such silica precursors, a thick silica layer is formed (Figure 6b). TG-DTA data for the as-synthesized (a) and BTMS-treated (b) mesoporous Nb oxide are compared in Figure 7. The exothermal peak without weight loss, which indicates the crystallization temperature, shifts from 603 to 652 °C, due to the formation of the thick silica layer. The slight increase in the crystallization temperature from thin-layered to thick-layered silica is caused by further suppression of mass transfer of atoms in Nb oxide during crystallization. The other exothermal peak with a remarkable weight loss at around 550 °C in Figure 7b is due to the combustion of organic groups of BTMS. The increase in the crystallization temperature of BTMS-treated mesoporous oxides was observed for all the metal oxide samples examined, as summarized in Table 1. Crystallization of the BTMS-treated mesoporous oxides was performed at

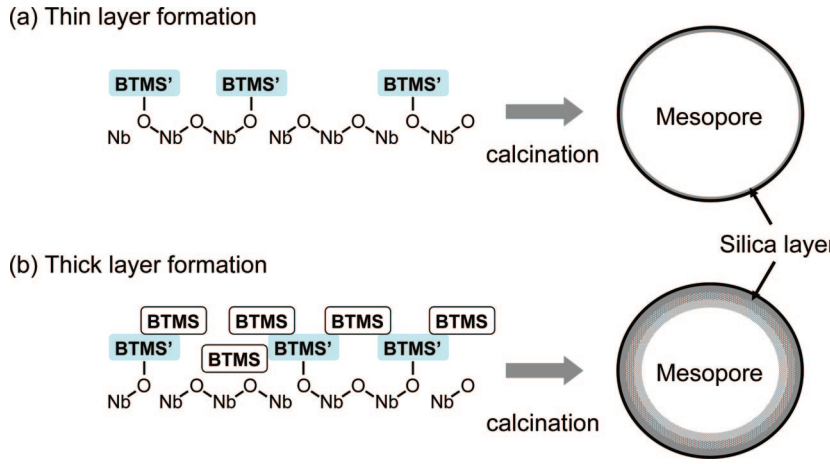

Figure 6. Schematic illustration of (a) thin layer and (b) thick layer silica formation by BTMS treatment.

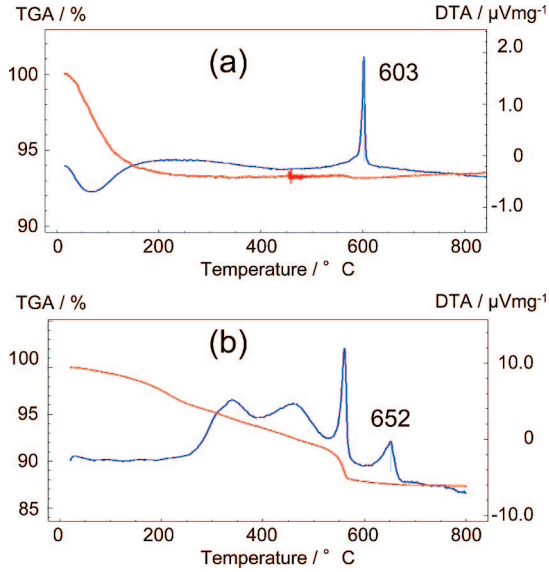

Figure 7. Comparison of TG-DTA data of (a) as-synthesized and (b) BTMS-treated amorphous mesoporous Nb_2O_5.

Table 1. Change in Crystallization Temperature upon BTMS Treatment

	crystallization temperature (°C)	
mesoporous metal oxides[a]	as-synthesized	BTMS-treated
Nb_2O_5	603	652
Ta_2O_5	770	845
$(Nb, Ta)_2O_5$	696	795
$MgTa_2O_6$	748	838
Al_2TiO_5	783	820
$TiZr_2O_6$	718	807
$TiNb_2O_6$	647	691

[a] Chemical compositions follow resulting crystallized phases.

the temperatures shown in Table 1 for periods of 1 or 3 h. Removal of the silica layer after crystallization of the metal oxides was conducted by several treatments (1–20 min each) with aqueous sodium hydroxide solution at 100 °C under a pH of 12–14. The extent of silica elimination was confirmed by elemental analyses (energy-dispersive X-ray spectroscopy, EDS) using a TEM apparatus. The averaged-silicon content of 10 particles was less than 2% of the total metal element content, except for the Ta-containing material. (The characteristic peak of Si appears at the same energy as that of Ta.) Thus, the presence of adsorbed BTMS and excess

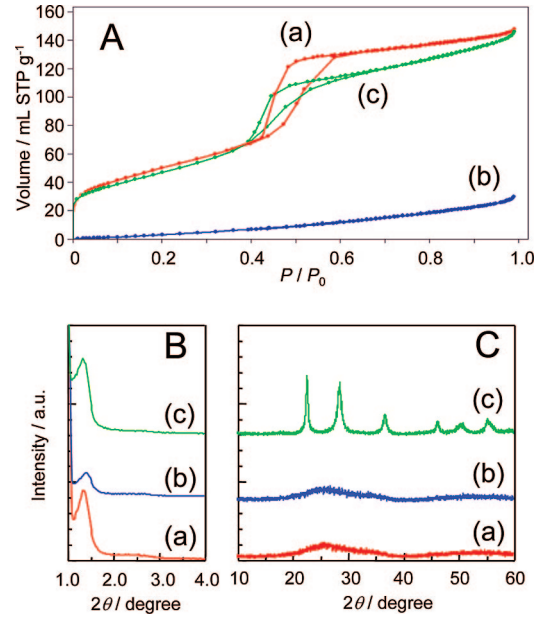

Figure 8. (A) N_2 adsorption–desorption isotherms and (B) small- and (C) wide-angle XRD patterns of mesoporous Nb_2O_5 samples; (a) amorphous, (b) BTMS-treated, and (c) silica-removed crystallized mesoporous final product.

BTMS-related materials (probably dimer, but not identified) is the key for the formation of sufficiently strong thick silica reinforcement.

Figure 8 shows comparisons of the N_2 adsorption–desorption isotherms and XRD patterns for amorphous (a) and BTMS-treated (b) mesoporous Nb oxides together with those of the crystallized and silica-removed mesoporous Nb oxide (c). The sorption data evidence a considerable amount of silica precursors are filled into the mesopores, resulting in the disappearance of remarkable N_2 uptake at $P/P_0 = 0.4$–0.6 for the BTMS-treated sample. The final product, crystallized mesoporous Nb oxide, which is obtained by silica etching after crystallization, demonstrates a similar sorption result (Figure 8A, c) to that of the amorphous precursor (Figure 8A, a), in addition to a similar peak in the small-angle XRD pattern (Figure 8B, a and c). Thus, the original 2D-hex mesoporous structure is expected to be maintained after crystallization using the present method, where confirmation of the conversion from an amorphous to a crystalline solid

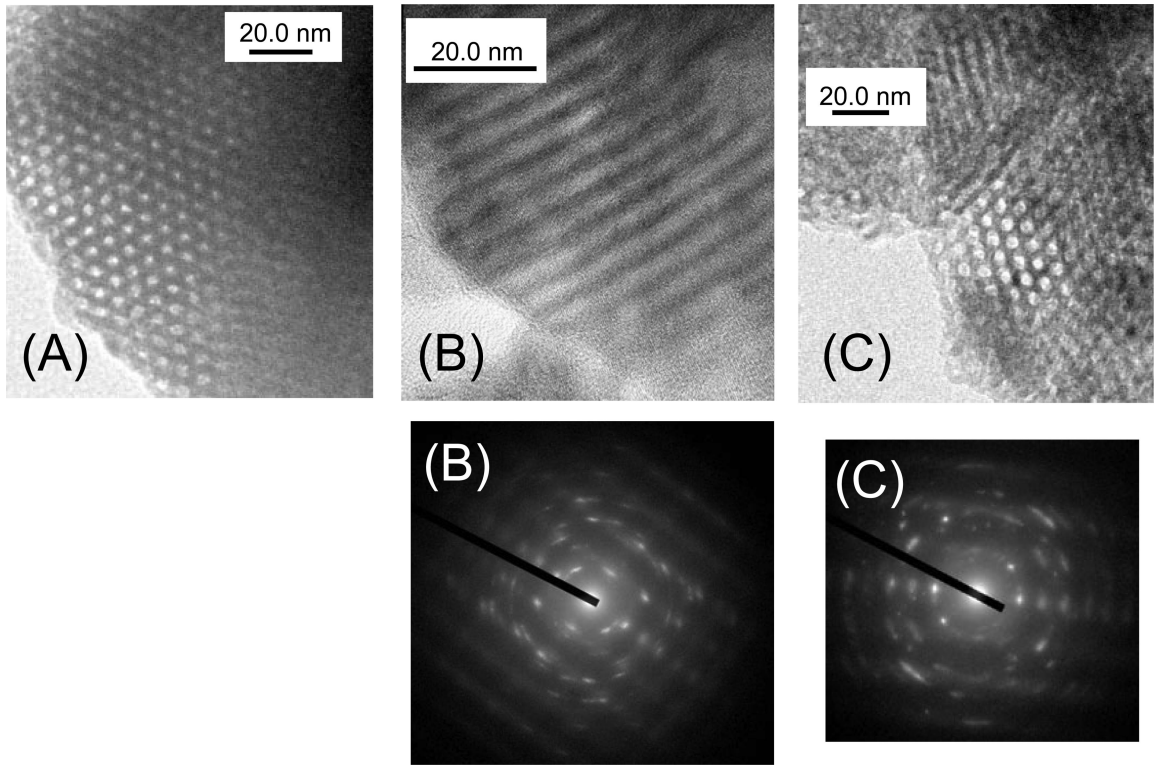

Figure 9. TEM images and ED patterns of mesoporous Nb_2O_5 samples; (a) BTMS-treated amorphous; (b) TEM and (d) ED after crystallization; and (c) TEM and (e) ED after silica removal.

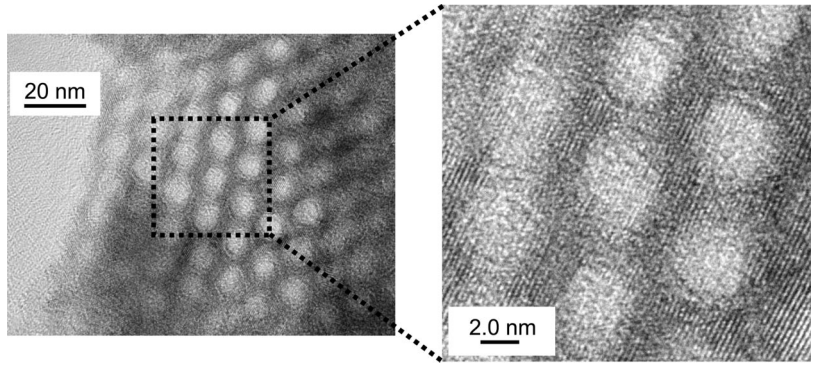

Figure 10. High-resolution TEM images of crystallized mesoporous Nb_2O_5.

is supported by the change in the wide-angle XRD patterns. To identify the origin of mesopores in the crystalline material, i.e., the relation between inorganic crystals and spaces, we examined high-resolution TEM and ED patterns. Figure 9 shows TEM images of BTMS-treated amorphous 2D-hex (A), BTMS-treated and crystallized (B), and further silica-removed (C) mesoporous Nb oxide samples. The elemental ratios of Nb/Si in the TEM areas shown in Figures 9A−C are 0.43, 0.34, and 0.02, respectively. The TEM images indicate the preservation of the original 2D-hex mesoporous structure. The spot ED patterns (Figures 9D and E) obtained in 50 nm diameter areas from the TEM images evidence the presence of some single-crystal phases, but not complete polycrystals, which are characterized by ring ED patterns. Thus, the pores in the finally crystallized Nb oxide are not attributed to spaces among nanoparticles, but to pores in crystalline domains, although a whole particle is not a single crystal. To disclose whether a single-crystalline phase can involve an ordered mesoporous structure originated from a starting amorphous material, we observed high-resolution images, one of which is shown in Figure 10. A single-crystalline domain in approximately 30 nm every direction certainly involves a 2D-hex mesoporous structure. Thus, single crystals are considered to sinter with large contact areas, resulting in retention of the original ordered mesoporous structure.

Changes in physicochemical properties of amorphous mesoporous metal oxides after crystallization, with and without BTMS-treatment, are compared in Table 2. The chemical compositions of the mixed oxides, described by the chemical formulas in the left column of Table 2, correspond to those determined by wide-angle powder XRD patterns of the crystallized materials, the ratios of which were adjusted by the amounts of metal precursors.[14] The absence of phase separation in crystallized mixed oxides, both with and without silica reinforcement, indicates homogeneous

Table 2. Change in Physicochemical Properties of Mesoporous Oxides upon Crystallization with the BTMS Method

mesoporous metal oxides[a]		surface area (m^2g^{-1})	pore size (nm)	pore volume (mL g^{-1})	d (100) (nm)
Nb_2O_5	(a)	183	5.1	0.30	6.0
	(b)	175	5.7	0.29	6.6
	(c)	17		0.07	
Ta_2O_5	(a)	153	3.6	0.20	6.2
	(b)	131	3.1	0.20	6.5
	(c)	33		0.15	
$(Nb,Ta)_2O_5$	(a)	196	5.2	0.33	6.3
	(b)	141	4.9	0.20	6.3
	(c)	32		0.17	
Al_2TiO_5	(a)	375	5.6	0.93	7.6
	(b)	296	6.3	0.54	
	(c)	155	9.0	0.53	
$TiZr_2O_6$	(a)	208	5.2	0.33	6.8
	(b)	192	5.7	0.34	7.0
	(c)	38		0.22	
$TiNb_2O_6$	(a)	214	5.0	0.31	6.7
	(b)	129	5.2	0.15	6.3
	(c)	35	10.2	0.13	

[a] (a) Samples before crystallization, (b) BTMS-strengthened crystallized sample, and (c) crystallized sample by simple calcination in air.

mixing of the metal precursors in the mixed-oxide phases.[14] In the case of Nb oxide, the surface area and the pore volume of the original mesoporous material were preserved with BTMS treatment, whereas simple crystallization in air decreased the surface area by 1 order of magnitude and the pore volume to less than a quarter. Because the optimized BTMS treatment does not require surface hydroxyl groups, the same method is applicable for metal oxides with hydrophobic surfaces. One representative hydrophobic mesoporous metal oxide is Ta oxide.[22] Large dye molecules can preferentially adsorb into pores of mesoporous Ta oxide from aqueous solution.[23] After BTMS treatment and crystallization of mesoporous Ta oxide, the surface area was decreased to approximately 100 m^2 g^{-1}, which was then recovered to 131 m^2 g^{-1} by silica removal.[24] Pore volume and pore size are also decreased, because of the presence of BTMS related compounds or thick silica layer, before or after crystallization, respectively, but recover to the values given in Table 2 after silica removal. Crystallized mesoporous Nb−Ta oxide is obtained by the BTMS-treatment method, similarly to that prepared by carbon filling.[20] Comparing the carbon-filling and silica-coating methods for crystallizing mesoporous metal oxides, the latter is regarded as superior due to the mild operation conditions. Furthermore, silica coating can be applied for various materials as a general method, although the quality of the crystallized mesoporous material is similar in the case of Nb−Ta oxide.

Nonporous crystallized Ta oxide and Ta mixed oxides are known to be active photocatalysts under ultraviolet (UV) irradiation.[25–30] Therefore, various mesoporous Ta mixed oxides were prepared. Among the various combinations attempted, Mg−Ta oxide was successfully prepared with a 2D-hex mesoporous structure. The high photocatalytic activity for water decomposition of amorphous mesoporous Mg−Ta oxide[12,13] attracted our attention, as improvement of the activity was expected after crystallization. However, the silica-coating method was not effective for mesoporous Mg−Ta oxide. N_2 sorption data and XRD patterns of amorphous mesoporous Mg−Ta oxide (Mg:Ta = 1:2) and crystallized $MgTa_2O_6$, with and without BTMS treatment, are shown in Figure 11. Although crystallization of amorphous mesoporous Mg−Ta oxide (114 m^2 g^{-1} surface area, 4.4 nm pore size, and 0.30 mL g^{-1} pore volume) in air decreases the surface area to 47 m^2 g^{-1}, and interparticle spaces are observed as an adsorption uptake at P/P_0 = 0.7–0.9, 1 in Figure 11A, that after BTMS treatment results in a drastic decrease in surface area to 15 m^2 g^{-1}, as estimated from Figure 11A, b. It is noted that the N_2 sorption data are the same for the samples before and after the three alkaline treatments at pH 14 and 100 °C. Although the structural damage during crystallization seems to be more serious for the BTMS-treated sample from Figure 11A, this conclusion is not reasonable and not coincident with the XRD results; the crystalline features of the two crystallized samples are almost the same (Figure 11C), but the small-angle XRD pattern of BTMS-treated crystallized $MgTa_2O_6$ indicates the presence of an ordered mesoporous structure (Figure 11B, b). A high-resolution TEM image of BTMS-treated and crystallized $MgTa_2O_6$ (Figure 11D) clarifies the existence of a 2D-hex ordered mesoporous structure in the crystalline phases (see lattice fringes), together with an unclear image inside and outside the observed particle. Thus, the silica coating is not removed by alkaline treatment (pH 14) even at 100 °C, and is most probably due to the formation of $SiTa_2O_7$ on the surface, although confirmation of this assumption by EDS is not available because of the overlap of Ta and Si signals.

Thermal stabilization of amorphous walls is achieved by mixing tri-, tetra- or penta-valent metal (Al, Zr, or Nb) with Ti in the oxide phase, which provides amorphous mesoporous materials even after the removal of SDA by calcination at 500 °C.[14] Thus-prepared Ti mixed oxides are treated with BTMS before crystallization, followed by the removal of silica. As found in Table 2, the silica coating effectively maintains the original structure, as represented by retention of the surface area and pore size in comparison with those of the as-crystallized materials. The decrease in pore volume in the crystallized materials, produced by both methods from corresponding amorphous precursors, is ascribed to the increase in density upon crystallization. It was noticed that the as-crystallized samples show similar pore volume to those of BTMS-treated samples because of the formation of nanocrystalline assemblies responsible for larger pores. A series of mesoporous Ti mixed oxides tend to consist of small crystalline domains, compared with the Nb and Ta oxides. The results of a structural analysis of mesoporous Ti−Zr oxide as an example are summarized in Figure 12. Although the crystalline state is regarded as the same for both crystallized materials, with and without BTMS treatment before crystallization (Figure 12C), a difference appears in the small-angle region; a peak at 1.0–2.0°, originating from a mesoporous structure, remains only for the BTMS-treated sample, as shown in Figure 12B. Figure 12A supports the preservation of the original mesoporous structure with the aid of the silica layer formation, even after crystallization, whereas the as-crystallized sample loses the given mesoporous structure in its crystalline solid phase. The TEM image

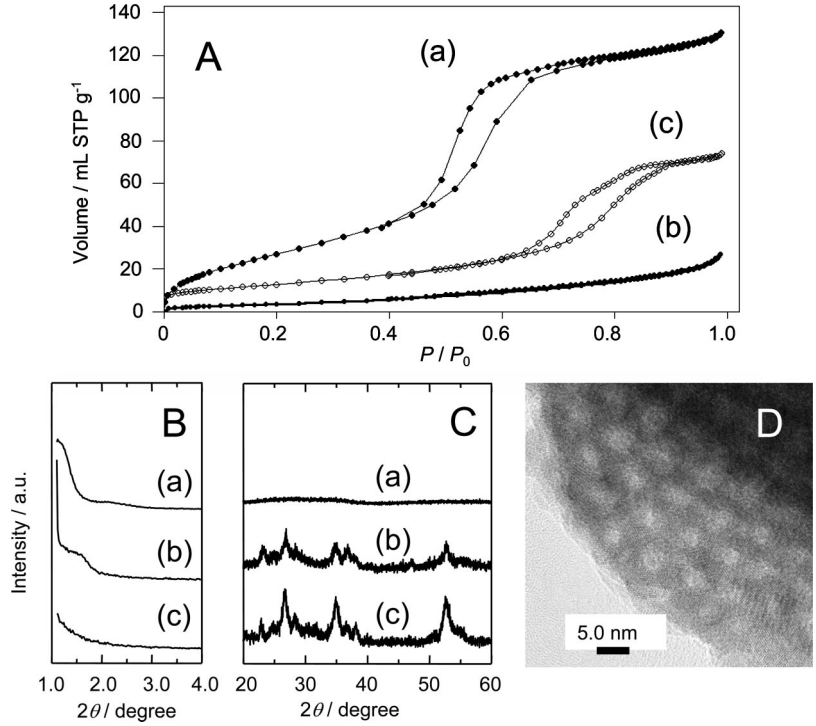

Figure 11. (A) N_2 adsorption–desorption isotherms, and (B) small- and (C) wide-angle XRD patterns of mesoporous $MgTa_2O_6$ samples; (a) amorphous precursor, (b) BTMS-treated and crystallized product after alkaline treatment, and (c) as-crystallized sample. (D) High-resolution TEM image for sample (b).

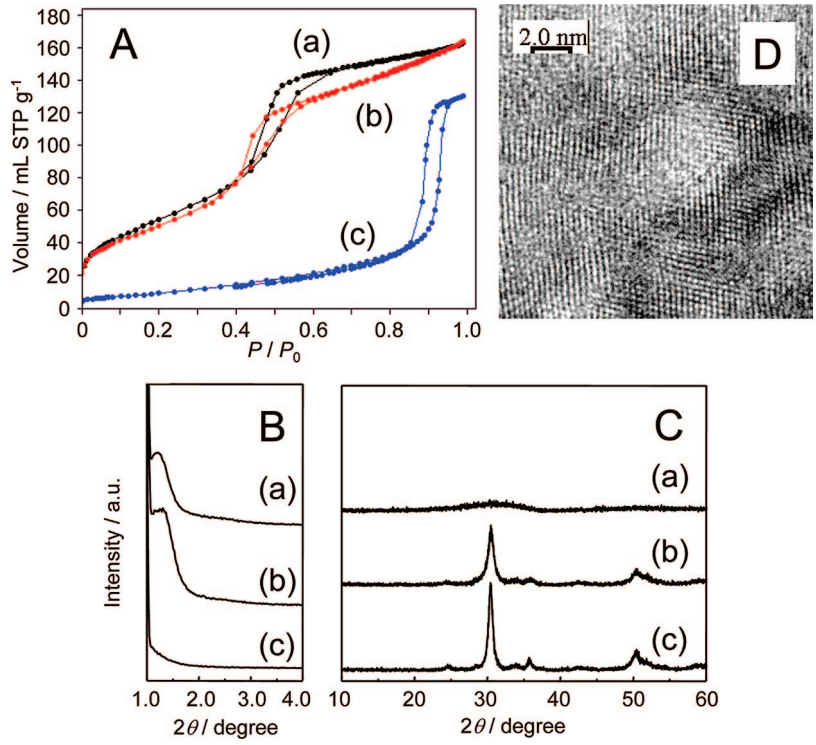

Figure 12. (A) N_2 adsorption–desorption isotherms, (B) small- and (C wide-angle XRD patterns of mesoporous $TiZr_2O_6$ samples; (a) amorphous, (b) BTMS-treated and crystallized product after silica removal, and (c) as-crystallized sample. (D) High-resolution TEM image for sample (c).

in Figure 12D consists of some single crystal domains in various directions and involves mesopores. Thus, it is considered that mesopores are present in the crystallized $TiZr_2O_7$ phase, in which single crystal patches are sintering with close face contact.

4.3. Silica Coating by TMOS-CVD. Silica coating was performed using less-complicated compounds than BTMS. With the information gained during optimization of the BTMS treatment, accumulation of tetramethoxysilane (TMOS) by chemical vapor deposition (CVD) was expected to form a thick silica layer on the surface. The thin silica layer, which is formed by the reaction of TMOS with surface hydroxyl groups, does not maintain the original structure after crystallization of the mesoporous metal oxide, similarly to the case

Table 3. Physicochemical Properties of Mesoporous Ta Oxides

	surface area (m^2 g^{-1})	pore volume (mL g^{-1})	pore size (nm)	repeat distance (nm)
(a)as-crystallized Ta oxide	20	0.13		
(b)amorphous precursor	163	0.30	4.8	6.22
(c)TMOS-treated mesoporous Ta oxide	169	0.30	4.5	6.59
(d)(c) after crystallization	96	0.17	3.7	6.59
(e)(d) after alkaline treatment	115	0.22	3.7	5.73

of the BTMS treatment. This TMOS-CVD accumulation method was optimized using mesoporous Ta oxide, a hydrophobic material with lesser amount of surface hydroxyl groups, for the purpose of improving the photocatalytic activity by crystallization, as well as further modification by nitridation for the visible light response. After evacuation pretreatment at 250 °C TMOS-CVD was performed five times at 200 °C for 1 min each time with evacuation in every interval, followed by adsorption and evacuation of water twice at the same temperature. This cycle was repeated four times, and the final set of TMOS-CVD cycle with five times was accomplished without further water treatment. Repetition of the TMOS-CVD process is used to include a certain amount of adsorbed TMOS molecules each time, and these molecules are hydrolyzed by successive water supply to form hydroxyl groups. A portion of the hydroxyl groups are dehydrated to form the silica layer, and some remaining hydroxyl groups reacted with TMOS provided in the next cycle. The optimum conditions for TMOS treatment depend on the amount of surface hydroxyl groups on the mesoporous oxides: a cycle of single supply of TMOS and water forms a silica monolayer on the sufficiently hydrated silica surface in a stepwise manner.[31] However, the hydrophobicity of mesoporous Ta oxide[22,23] requires such severe TMOS treatment conditions for the formation of a silica layer.

After TMOS-CVD treatment, an increase in the crystallization temperature was observed in TG-DTA, similar to that for BTMS treatment. The silica layer was removed after crystallization using the same alkaline treatment as mentioned above. Changes in the physicochemical properties of mesoporous Ta oxide after each procedure are summarized in Table 3. The surface area and pore volume of the sample after TMOS treatment do not differ from that of the sample before TMOS treatment, because the amount of adsorbed silica is small. However, the surface area and pore volume are decreased after calcination at high temperature for crystallization because of the increase in the density of the sample upon crystallization. The removal of silica results in the recovery of both the surface area and pore volume, supporting the change of the structure inside the mesopores. Small- and wide-angle XRD patterns, together with N_2 adsorption–desorption isotherms of the resulting crystallized mesoporous Ta oxide, are shown in Figure 13. The coexistence of periodically ordered mesopores and crystalline features is confirmed by the XRD patterns, and the sorption data indicate the presence of uniform mesopores. The high-resolution TEM image in Figure 14A demonstrates mesopores (white lines) and lattice fringes crossing the mesopores at the same area. The ED pattern (Figure 14B) measured from the area shown in Figure 14A reflects the presence of ordered structures at simultaneous nanometer and angstrom scales; each spot attributed to a crystalline diffraction consists of a pattern derived from the ordered arrangement of mesopores (layer-pattern) observed in Figure 14A. The SEM image of the crystalline mesoporous Ta oxide (Figure 14C) further supports the preservation of the original long-range 2D-hex ordered mesoporous structure in one direction of a particle. Thus, it is concluded that the crystalline mesoporous Ta oxide prepared through TMOS-CVD method is not a mixture of ordered amorphous mesoporous material and nonporous crystalline particles, but crystalline material with mesopores arranged in single-crystal domains.

5. Photocatalysis of Mesoporous Ta Oxide with Crystalline Structure

Applications of crystalline mesoporous metal oxides are less reported than those of amorphous metal oxides. In spite of nanocrystalline materials, where inorganic phases are not continuous through mesopores, applications of crystalline mesoporous TiO_2 and Al_2O_3 are of importance and have recently been reviewed.[3,4] Various applications of nanostructured TiO_2, with and without crystalline phases, are utilized as photochromic devices, photocatalysts, sensors, and so on, sometimes with appropriate modifications.[4] The superiority of crystallized mesoporous Al_2O_3 over conventional nonporous samples as a catalyst–support are summarized in a review article.[3] Activity approximately twice as high was observed for a hydrodesulfurization reaction when Mo oxide catalyst was supported on mesoporous Al_2O_3 rather than a commercial catalyst.[32] In addition, Re oxide dispersed on mesoporous Al_2O_3 is found to be more active and selective for the metathesis of terminal and inner olefins, as compared to γ-Al_2O_3.[33] As one of the applications of crystalline mesoporous metal oxides prepared by the reinforcement method, the photocatalytic activity of mesoporous Ta_2O_5 was examined.

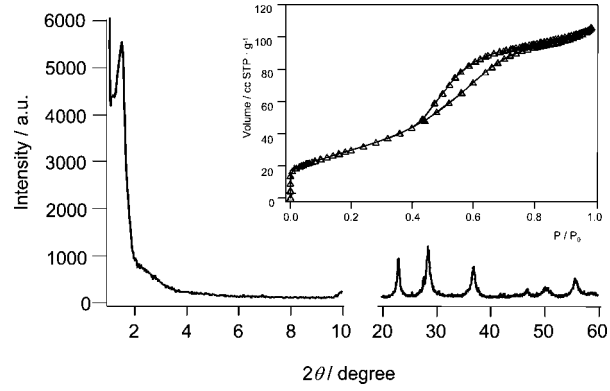

Figure 13. XRD pattern and N_2 adsorption–desorption isotherms (inset) for crystallized mesoporous Ta_2O_5 with BTMS support after the removal of SiO_2.

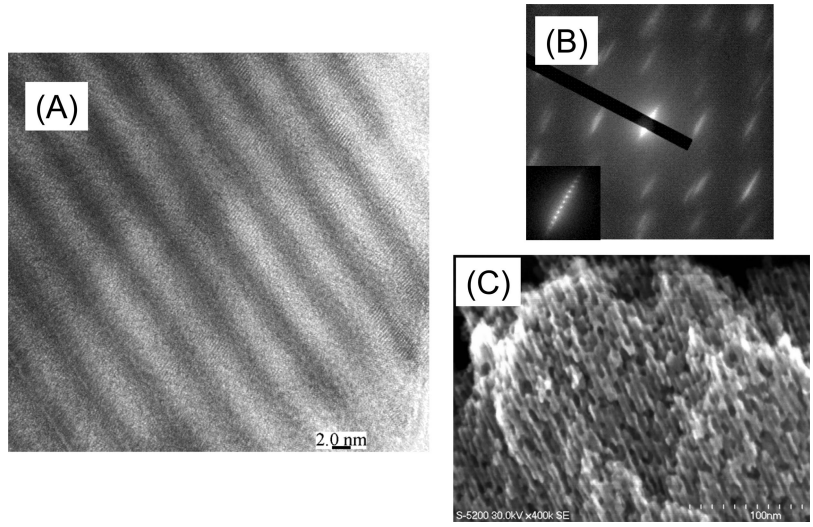

Figure 14. (A) High-resolution TEM image, (B) ED pattern, and (C SEM image for crystallized mesoporous Ta_2O_5 with BTMS support after removal of SiO_2.

Table 4. Photocatalytic Activity of Ta Oxides for Overall Water Decomposition

						activity[b] (μmol h^{-1})	
sample	mesopores[a]	crystalline structure[a]	wall thickness (nm)	pore size (nm)	NiO (wt %)	H_2	O_2
A	X	X			1.0	125	43
B	X	○			1.0	389	194
C	○	X	1.2	2.6	4.0	515	272
D	○	X	2.9	4.8	3.0	383	171
E	○	○	3.7	3.7	3.0	1852 (3364)	667 (1633)

[a] Cross and circle represent absence and presence, respectively. [b] Activities are measured for 5 h, whereas those in parentheses are measured in initial 1 h.

One of the interesting characteristics of mesoporous Ta oxide is its photocatalytic activity for water decomposition. It was found that mesoporous Ta[34,35] and Mg−Ta[12,13] oxides exhibit high photocatalytic activity for overall water decomposition under UV irradiation, regardless of their amorphous wall structure. This is attributed to the short distance from the bulk to surface, which is derived from mesoporous structure, so that photoexcited electrons and holes efficiently migrate onto the surface with less opportunity for deactivation, even though their mobility is lower in an amorphous phase than in a crystalline phase. This interpretation is supported by the dependence of the photocatalytic performance on the thickness of the wall of amorphous mesoporous Ta oxides; a thinner wall has higher activity.[27] There is also interest regarding the effect of crystallization of the pore walls, which promotes the mobility of electrons and holes. Therefore, the photocatalytic performance of crystalline mesoporous Ta oxide was examined and compared with other Ta oxides.

For the construction of an efficient photocatalytic system, the catalyst was modified with a cocatalyst, which is usually the active site for H_2 evolution (reduction). As a cocatalyst, NiO is superior to RuO_2 and Rh−Cr for both amorphous and crystalline mesoporous Ta oxide. Therefore, NiO-loaded samples were first pretreated by H_2 reduction at 500 °C for 2 h, followed by reoxidation in O_2 at 200 °C for 1 h. This pretreatment changes the loaded NiO to metallic Ni on the inside and subsequently covers this by a NiO layer on the outside, which functions as an active site for H_2 evolution, in addition to avoiding the reverse reaction.[36–39] The optimum amount of NiO is dependent on the sample, and is usually optimized experimentally, as the amounts shown in Table 4 are.

The photocatalytic activities of various Ta oxides are compared in Table 4 with brief structural properties. It should be noted that photocatalytic activity depends on the number of photons irradiated to the solid. Thus, the thickness of the inorganic phase is of greater importance than the surface area. Samples A and B are amorphous and crystalline nonporous Ta oxides, respectively; therefore, there are no data for wall thickness or pore size. Samples C, D, and E are mesoporous Ta oxides; C and D consist of amorphous inorganic phases with different wall thickness, whreas E was obtained by crystallization of sample D through BTMS treatment. The thin pore walls of sample C were destroyed by thermal treatment even with the presence of a silica layer. Comparison of nonporous Ta oxides, with and without crystalline structure, clearly indicates the significance of crystallinity for photocatalytic reactions. In addition, over nonporous amorphous sample A, H_2 and O_2 were not evolved in stoichiometric ratio, indicating that the catalytic cycle did not proceed smoothly. On the other hand, two types of amorphous mesoporous Ta oxide with different wall thicknesses could split water into H_2 and O_2 with a 2:1 ratio by UV light irradiation. Being different from nonporous material, mesoporous Ta oxides are regarded as suitable for the present photocatalytic reaction, regardless of the amorphous wall structure. From the two amorphous mesoporous Ta oxides (C and D), the thin-walled sample exhibited much higher activity than the other, supporting the consideration

that a thin inorganic phase is advantageous for photocatalytic reactions because of the short path length for excited electrons and holes to reach the surface with less possibility for recombination. Therefore, catalytic performance equivalent to the crystalline nonporous Ta oxide was observed even for the less active thick-walled sample D. Preliminary results for the crystallized mesoporous Ta oxide are also shown in Table 4 (E). Obviously, the catalytic performance is enhanced, even when the wall thickness is increased from the corresponding amorphous material (D). However, evolution of O_2 is suppressed, similarly to sample A. The values in parentheses shown in Table 4 are the activity measured during the initial first hour, which were extremely high and in stoichiometric ratio. Therefore, some kind of deactivation occurs during the initial reaction period. Although the details of the reaction and improvement of the catalyst are still under examination, the high potential of crystallized mesoporous Ta oxide for a photocatalytic reaction is confirmed.

6. Direct Syntheses of Crystallized Mesoporous Metal Oxides

Some mesoporous metal oxides are crystallized at a higher temperature than that required for complete template removal by calcination. Consequently, the original ordered mesoporous structure is not successfully preserved after removal of the template. In this section, strategies for direct synthesis of crystalline mesoporous metal oxides with low crystallization temperature are introduced.

Optimization of the general method is first introduced, where intentional crystallization is carefully conducted during the temperature increase for template removal. In this method, the calcination conditions are controlled by considering the rate of surfactant combustion, extent of local thermal induction due to combustion, the rate of nucleation, the rate of crystal growth, and so on. Pioneering research on the direct crystallization were conducted using thin films of mesoporous TiO_2 and ZrO_2,[40] and yittoria−zirconia and ceria−zirconia.[41] The amorphous mesoporous films were prepared by the evaporation-induced self-assembly (EISA) method under the controlled atmospheric humidity. Careful observations of the films under the tuned preparation condition were performed by small-angle X-ray scattering (SAXS), XRD and TEM. In addition to the changes in mesoporous structure at low temperatures (<100 °C), crystallization processes, resulting in nanocrystalline mesoporous thin films, were examined. On the basis of activation energies and rate constants, the optimal conditions for producing highly crystalline walls with minimal loss of nanometer-scale order in the mesoporous Ti oxide film have been found to involve thermal activation for short times at high temperatures. It has been suggested that rapid thermal annealing processes are vital for the successful production of crystallized mesoporous titania, because the crystallization rate is far greater than the rate of nanoscale-order deterioration.[42] Some mesoporous thin films, consisting of highly crystallized transition metal oxides, have been prepared in a similar manner,[43] such as Nb_2O_5, Ta_2O_5, MoO_3, V_2O_5, and SnO_2.[44,45] These transition metal oxide films maintain the original mesostructures with the aid of a thermally resistant SDA, named KLE ($H(CH_2CH_2CH_2\ (CH)CH_2CH_3)_{89}(OCH_2)_{79}OH$), which are present inside the pores at higher temperature range than that of generally used P123 SDA.

The most frequently studied material is Ti oxide, because this material is used in various applications such as photocatalysis[46] and energy conversion.[47] The crystallization behavior of mesoporous Ti oxide has been systematically examined using in situ XRD analysis of films.[43] In nonporous Ti oxide systems,[48] amorphous grains are crystallized into anatase, rutile, or a mixture of these two phases, depending on the preparation conditions and the initial particle size. In a mesoporous titania system, the amorphous phase transforms to the metastable anatase phase after heating at around 400 °C, and further heating at 900–1000 °C leads to the formation of the rutile structure as the titania grains fuse to form larger particles. It is worth noting that nanoanatase crystalline particles were formed within mesoporous network of the aerosol-generated titania particle by thermal treatment at 350 °C.[49] Although gradual pore expansion and crystal growth upon increasing temperature of calcination of mesoporous Al_2O_3 was observed,[3] the recently reported submicrometric spherical Al_2O_3 power includes both three-dimensional ordered mesoporous structure and γ- Al_2O_3 crystalline phase after calcination at 900 °C.[50] This was elaborated by aerosol formation in combination with EISA. The γ-Al_2O_3 with high surface area (134 m^2g^{-1}) and porosity (0.34 mL g^{-1}) as well as uniform pore size (12.5 nm) would be advantageous in the fields of catalysis, environment and separation. Powders were successfully obtained for Cr oxide using a similar approach.[47] Crystallized mesoporous Cr_2O_3, prepared by a neutral templating route with carefully controlled experimental conditions shows exceptionally high ability for the removal/oxidation of volatile organic compounds (VOCs) (toluene, acetaldehyde), whereas the amorphous mesoporous Cr_2O_3 is inactive.[51] Control of the rate of precursor hydrolysis, condensation of metal species, and slow crystallization are important prerequisites for enhanced framework cross-linking that leads to a stable mesoporous structure. The obtained mesoporous Cr_2O_3 has a high surface area (78 m^2 g^{-1}) and uniform mesopores (7.9 nm) and is a highly ordered three-dimensional mesoporous system.

In one strategy, P_2O_5 glass is used as a gluelike material, in order to stabilize the formed nanoparticles in the same positions. A synthetic methodology is proposed for producing an ordered mesoporous nanocomposite with a crystalline framework,[52] where highly ordered and crystallized mesoporous TiO_2−P_2O_5 and TiO_2−P_2O_5−M_xO_y (Li_2O, CuO, NiO, Fe_2O_3, MnO_2, SnO_2, and WO_3) are produced. The nanocomposite design is composed of a large number of functional nanocrystals such as TiO_2 and smaller quantities of the glass phase (P_2O_5). The nanocrystals, which govern the properties of the nanocomposite, are designed as basic building blocks of the mesopores. The glass phase, which is thermodynamically stable as an amorphous phase, is designed to provide predictable and controllable properties as a good host material, to help in the formation and maintenance of the three-dimensional network, and to act as a "glue" among the nanocrystals.

Hard-templating pathways have been recently reported, where ordered mesoporous silicas (SBA-15, SBA-16, KIT-6, etc.) and mesoporous carbon (CMK-3) are used as second-generation templates to synthesize ordered mesostructured transition metal oxides.[53] This method is based on the impregnation of sufficient amounts of metals or metal ions into the mesopores of the hard-template, followed by the oxidation of metals or the thermolysis of metal ions by calcination treatment. A one-step nanocasting route is used to prepare highly ordered single-crystal In oxide nanowire arrays.[54,55] Because of the low melting point of In oxide, the mesopores are completely filled with indium nanoparticles that can be aggregated in a certain segment to grow indium nanowires. The nanowires are further oxidized to form single-crystal In oxide. The BET surface area and the pore volume of the resulting material are 170 $m^2\ g^{-1}$ and 0.45 mL g^{-1}, respectively.

An efficient preparative protocol for mesostructured Os oxide is also reported, where the capillary insertion of molten organometallic precursors toward the mesopores of MCM-48 is utilized.[56] The resulting material exhibits high catalytic activity and excellent reusability in oxidative cleavage and dihydroxylation of alkenes. Mesoporous Mg oxide is also prepared through a hard-templating pathway using mesoporous carbon aerogel as a template and magnesium nitrate solution as the Mg oxide precursor.[57] The primary Mg oxide particles obtained have an almost spherical shape, and are connected to form a three-dimensional network structure. The surface area and pore volume can reach up to 150 $m^2\ g^{-1}$ and 0.73 mL g^{-1}, respectively. By using mesoporous silicas such as SBA-15 and KIT-6 as hard-templates, we fabricated mesostructured single crystals of Cr and Co oxides (Cr_2O_3 and Co_3O_4).[58,59] The surface area and pore volume of mesostructured Cr_2O_3 are 92 $m^2\ g^{-1}$ and 0.17 mL g^{-1}, and those of Co_3O_4 are 74 $m^2\ g^{-1}$ and 0.46 mL g^{-1}, respectively. A significant confinement effect is observed inside the mesopores. Because of the different thermodynamics in a space-restricted environment, change in the stability of intermediate phases results in a change in the types of observable phases during decomposition of the metal nitrates. Additionally, the crystallization temperature and rate of crystal growth of the metal oxides are decreased inside the pore-channels. Mesostructured α-Fe_2O_3 with crystalline walls was synthesized using KIT-6 as hard-template.[60] The resulting material exhibits single crystal-like order throughout the walls of each particle, which is different from orientationally disordered polycrystals. This material is quite similar to that shown in Figures 9 and 12, which was prepared by the reinforcement method described in Section 2.4. In the same system, an interesting phase transition occur by reducing mesoporous α-Fe_2O_3 to Fe_3O_4 spinel, then to γ-Fe_2O_3 by oxidation, while preserving the ordered mesostructure and crystalline walls throughout.[61] Such solid−solid transformations demonstrate the stability of the mesostructural to structural phase transitions, from the hexagonal close packed oxide subarray of α-Fe_2O_3 to the cubic close packed subarray of Fe_3O_4 spinel and γ-Fe_2O_3. This is the first synthesis of mesoporous Fe_3O_4 or any reduced mesoporous iron oxide, which is difficult to carry out directly. As a last example, mesostructured Cu oxide with a highly ordered 2D-hex structure was synthesized using CMK-3 carbon as a template.[62] The surface area, pore volume, and pore size are 149 $m^2\ g^{-1}$, 0.22 mL g^{-1}, and 5.5 nm, respectively, and the resulting material has potential applications in catalysis or lithium ion batteries.

7. Conclusion

Preparation of periodic crystalline mesoporous metal oxides using structure-strengthening materials was introduced. Although carbon and SiO_2 were used as reinforcements, there should be other more suitable materials. When crystalline mesoporous metal oxides with large single-crystal domains containing ordered mesoporous structure can be generally prepared, they are expected to be applied in various fields due to their high performance. The emergence of new types of materials is not only beneficial for applications that are closely linked to our daily life, but also enable us to examine fundamental aspects of the physical chemistry of solids. Change in the uniform thickness of pore walls of crystalline mesoporous metal oxides allows us to examine the dependence of electron conductivity, sensing capacity, and magnetic properties in a defined distance on wall thickness in detail, because of rigidly separated inorganic phases. Such dependence is only approximately understood using conventional metal oxide powders. Thus, fine control of the physical properties of materials with high yield would be a significant requirement for both applications and fundamental studies. In addition, the development of crystalline mesoporous materials, which are prepared by a method based on totally new synthesis concept, is highly expected.

Acknowledgment. This work is partly supported by a Kakenhi Grant-in-Aid for Scientific Research (B) from CREST (Core Research for Evolutional Science and Technology) of JST (Japan Science and Technology).

References

(1) Chang, R. In *Chemistry*, 9th ed.; McGraw-Hill: New York, 2007; p 471.
(2) Antonelli, D. M.; Nakahira, A.; Ying, J. Y. *Inorg. Mater.* **1996**, *35*, 3126.
(3) Cejka, J. *Appl. Catal., A* **2003**, *254*, 327.
(4) Chen, X.; Mao, S. S. *Chem. Rev.* **2007**, *107*, 2891.
(5) Fujita, S.; Inagaki, S. *Chem. Mater.* **2008**, *20*, XXX–XXX.
(6) Tao, Y.; Kanoh, H.; Abrams, L.; Kaneko, K. *Chem. Rev.* **2006**, *106*, 896.
(7) van Donk, S.; Janssen, A. H.; Bitter, J. H.; de Jong, K. P. *Catal. Rev.* **2003**, *45*, 297.
(8) Yang, P.; Zhao, D.; Margolese, D. I.; Chmelka, B. F.; Stucky, G. D. *Nature* **1998**, *396*, 157.
(9) Yang, P.; Zhao, D.; Margolese, D. I.; Chemelka, B. F.; Stucky, G. D. *Chem. Mater.* **1999**, *11*, 2813.
(10) Schüth, F. *Chem. Mater.* **2001**, *13*, 3184 and references therein.
(11) Katou, T.; Lu, D.; Kondo, J. N.; Domen, K. *J. Mater. Chem.* **2002**, *12*, 1480.
(12) Uchida, M.; Kondo, J. N.; Lu, D.; Domen, K. *Chem. Lett.* **2002**, 498.
(13) Kondo, J. N.; Uchida, M.; Nakajima, K.; Lu, D.; Hara, M.; Domen, K. *Chem. Mater.* **2004**, *16*, 4304.
(14) Kondo, J. N.; Yamashita, T.; Nakajima, K.; Lu, D.; Hara, M.; Domen, K. *J. Mater. Chem.* **2005**, *15*, 2035.
(15) Lee, B.; Lu, D.; Kondo, J. N.; Domen, K. *Chem. Commun.* **2001**, 2118.
(16) Lee, B.; Yamashita, T.; Kondo, J. N.; Lu, D.; Domen, K. *Chem. Mater.* **2002**, *14*, 867.
(17) Katou, T.; Lu, D.; Kondo, J. N.; Domen, K. *J. Mater. Chem.* **2002**, *12*, 1480.
(18) Kondo, J. N.; Katou, T.; Lu, D.; Hara, M.; Domen, K. *Stud. Surf. Sci. Catal.* **2004**, *154*, 951.
(19) Jun, S.; Joo, S. H.; Ryoo, R.; Kurk, M.; Jaroniec, M.; Liu, Z.; Ohsuna, T.; Terasaki, O. *J. Am. Chem. Soc.* **2000**, *122*, 10712.
(20) Katou, T.; Lee, B.; Lu, D.; Kondo, J. N.; Hara, M.; Domen, K. *Angew. Chem., Int. Ed.* **2003**, *42*, 2382.

(21) Wu, N.-L.; Wang, S.-Y.; Rusakova, I. A. *Science* **1999**, *27*, 1375.
(22) Lu, L.; Abe, R.; Kondo, J. N.; Maruya, K.; Domen, K.; Igarashi, N.; Tatsumi, T. *Chem. Lett.* **1998**, 869.
(23) Kondo, J. N.; Takahara, Y.; Lee, B.; Lu, D.; Domen, K. *Top. Catal.* **2002**, *19*, 171.
(24) Shirokura, N.; Nakajima, K.; Nakabayashi, A.; Lu, D.; Hara, M.; Domen, K.; Tatsumi, T.; Kondo, J. N. *Chem. Commun.* **2006**, 2188.
(25) Kudo, A.; Kato, H. *Chem. Lett.* **1997**, 867.
(26) Kato, H.; Kudo, A. *Chem. Phys. Lett.* **1998**, *295*, 487.
(27) Kato, H.; Kudo, A. *Catal. Lett.* **1999**, *58*, 183.
(28) Kato, H.; Kudo, A. *Chem. Lett.* **1999**, 1207.
(29) Kudo, A.; Kato, H.; Nakazawa, S. *J. Phys. Chem. B* **2000**, *104*, 571.
(30) Ishihara, T.; Nishiguchi, H.; Fukamachi, K.; Takita, Y. *J. Phys. Chem. B* **1999**, *103*, 1.
(31) Ishimaru, R.; Shibasaki, Y.; Hara, M.; Ueda, M.; Domen, K.; Kondo, J. N. *Chem. Lett.* **2005**, *34*, 596.
(32) Kaluza, L.; Zdrazil, M.; Cejka, J. *Catal. Commun.* **2002**, *3*, 151.
(33) Onaka, M.; Oikawa, T. *Chem. Lett.* **2002**, 850.
(34) Takahara, Y.; Kondo, J. N.; Takata, T.; Lu, D.; Domen, K. *Chem. Mater.* **2001**, *13*, 1194.
(35) Nakajima, K.; Lu, D.; Hara, M.; Domen, K.; Kondo, J. N. *Stud. Surf. Sci. Catal.* **2005**, *158B*, 1477.
(36) Domen, K.; Takata, T.; Hara, M.; Kondo, J. N. *Bull. Chem. Soc. Jpn.* **2000**, *73*, 1307.
(37) Takata, T.; Tanaka, A.; Hara, M.; Kondo, J. N.; Domen, K. *Catal. Today* **1998**, *44*, 17.
(38) Domen, K.; Ebina, Y.; Kondo, J. N. *Rev. Chem. Intermed.* **1994**, *20*, 895.
(39) Tanaka, A.; Kondo, J. N.; Domen, K. *Crit. Rev. Surf. Chem.* **1994**, *305*, 5.
(40) Crepaldi, E. L.; Soler-Illia, G. J.; de, A. A.; Grosso, D.; Sanchez, C. *New J. Chem.* **2003**, *27*, 9.
(41) Crepaldi, E. L.; Soler-Illia, G. J.; de, A. A.; Bouchara, A.; Grosso, D.; Durand, D.; Sanchez, C. *Angew. Chem.* **2003**, *115*, 361.
(42) Kirsch, B. L.; Richman, E. K.; Riley, A. E.; Tolbert, S. H. *J. Phys. Chem. B* **2004**, *108*, 12698.
(43) Brezesinski, T.; Groenewolt, M.; Pinna, N.; Amenitsch, H.; Antnietti, M.; Smarsly, B. M. *Adv. Mater.* **2006**, *18*, 1827.
(44) Urade, V. N.; Hillhouse, H. W. *J. Phys. Chem. B* **2005**, *109*, 10538.
(45) Brezesinski, T.; Fischer, A.; Iimura, K.; Sanchez, C.; Grosso, D.; Antnietti, M.; Smarsly, B. M. *Adv. Funct. Mater.* **2006**, *16*, 1433.
(46) Shibata, H.; Mukai, T.; Akita, T.; Ohkubo, T.; Sakai, H.; Abe, M. *Chem. Lett.* **2005**, *34*, 1696.
(47) Lancelle-Beltran, E.; Prené, P.; Boscher, C.; Belleville, P.; Buvat, P.; Sanchez, C. *Adv. Mater.* **2006**, *18*, 2579.
(48) Kumar, P. M.; Badrinarayanan, S.; Sastry, M. *Thin Solid Films* **2000**, *358*, 122.
(49) Grosso, D.; Soler-Illia, G. J.; de, A. A.; Crepaldi, E. L.; Charleux, B.; Sanchez, C. *Adv. Funct. Mater.* **2003**, *13*, 37.
(50) Boissere, C.; Nicole, L.; Gervais, C.; Babounneau, F.; Antonietti, M.; Amenitsch, H.; Sanchez, C.; Grosso, D. *Chem. Mater.* **2006**, *18*, 5238.
(51) Sinha, A. K.; Suzuki, K. *Angew. Chem., Int. Ed.* **2005**, *44*, 271.
(52) Li, D.; Zhou, H.; Honma, I. *Nat. Mater.* **2004**, *3*, 65.
(53) Schüth, F. *Angew. Chem., Int. Ed.* **2003**, *42*, 3604.
(54) Yang, H.; Shi, Q.; Tian, B.; Lu, Q.; Gao, F.; Xie, S.; Fan, J.; Yu, C.; Tu, B.; Zhao, D. *J. Am. Chem. Soc.* **2003**, *125*, 4724.
(55) Tian, B.; Liu, X.; Solovyov, L. A.; Liu, Z.; Yang, H.; Zhang, Z.; Xie, S.; Zhang, F.; Tu, B.; Yu, C.; Terasaki, O.; Zhao, D. *J. Am. Chem. Soc.* **2004**, *126*, 865.
(56) Lee, K.; Kim, Y.-H.; Han, S. B.; Kang, H.; Park, S.; Seo, W. S.; Park, J. T.; Kim, B.; Chang, S. *J. Am. Chem. Soc.* **2003**, *125*, 6844.
(57) Li, W.-C.; Lu, A.-H.; Weidenthaler, C.; Schüth, F. *Chem. Mater.* **2004**, *16*, 5676.
(58) Zhu, K.; Yue, B.; Zhou, W.; He, H. *Chem. Commun* **2003**, *24*, 98.
(59) Dickinson, C.; Zhou, W.; Hodgkins, R. P.; Shi, Y.; Zhao, D.; He, H. *Chem. Mater.* **2006**, *18*, 3088.
(60) Jiao, F.; Harrison, A.; Jumas, J.-C.; Chadwick, A. V.; Kockelmann, W.; Bruce, P. G. *J. Am. Chem. Soc.* **2006**, *128*, 5468.
(61) Jiao, F.; Harrison, A.; Jumas, J.-C.; Womes, M.; Chadwick, A. V.; Harrison, A.; Bruce, P. G. *J. Am. Chem. Soc.* **2006**, *128*, 12905.
(62) Lai, X.; Li, X.; Geng, W.; Tu, J.; Li, J.; Qiu, S. *Angew. Chem., Int. Ed.* **2007**, *46*, 738.

CM702176M